Holographic Observations of Centimeter-Scale Nonuniformities within Marine Stratocumulus Clouds

SUSANNE GLIENKE

Michigan Technological University, Houghton, Michigan, and Johannes Gutenberg University, and Max Planck Institute for Chemistry, Mainz, Germany

ALEXANDER B. KOSTINSKI AND RAYMOND A. SHAW

Michigan Technological University, Houghton, Michigan

MICHAEL L. LARSEN

College of Charleston, Charleston, South Carolina, and Michigan Technological University, Houghton, Michigan

JACOB P. FUGAL,[a] OLIVER SCHLENCZEK,[b] AND STEPHAN BORRMANN

Johannes Gutenberg University, and Max Planck Institute for Chemistry, Mainz, Germany

(Manuscript received 13 June 2019, in final form 4 October 2019)

ABSTRACT

Data collected with a holographic instrument [Holographic Detector for Clouds (HOLODEC)] on board the High-Performance Instrumented Airborne Platform for Environmental Research Gulfstream-V (HIAPER GV) aircraft from marine stratocumulus clouds during the Cloud System Evolution in the Trades (CSET) field project are examined for spatial uniformity. During one flight leg at 1190 m altitude, 1816 consecutive holograms were taken, which were approximately 40 m apart with individual hologram dimensions of 1.16 cm $\times$ 0.68 cm $\times$ 12.0 cm and with droplet concentrations of up to 500 cm^{-3}. Unlike earlier studies, minimally intrusive data processing (e.g., bypassing calculation of number concentrations, binning, and parametric fitting) is used to test for spatial uniformity of clouds on intra- and interhologram spatial scales (a few centimeters and 40 m, respectively). As a means to test this, measured droplet count fluctuations are normalized with the expected standard deviation from theoretical Poisson distributions, which signifies randomness. Despite the absence of trends in the mean concentration, it is found that the null hypothesis of spatial uniformity on both spatial scales can be rejected with compelling statistical confidence. Monte Carlo simulations suggest that weak clustering explains this signature. These findings also hold for size-resolved analysis but with less certainty. Clustering of droplets caused by, for example, entrainment and turbulence, is size dependent and is likely to influence key processes such as droplet growth and thus cloud lifetime.

1. Introduction

The spatial distribution of droplets in clouds affects the rate of droplet growth through collision–coalescence (e.g., Pruppacher and Klett 2010), radiative transfer through a cloud (e.g., Matsuda et al. 2012), the competition for water vapor during condensational growth (e.g., Srivastava 1989), and even the rate of the icing process on aircraft wings (e.g., Jameson and Kostinski 2000). While some work suggests cloud droplets can be distributed randomly in space (e.g., Scott 1967; Borrmann et al. 1993; Chaumat and Brenguier 2001), recent theoretical, numerical, and experimental studies argued for spatial "clustering" of the droplets (e.g., Uhlig et al. 1998; Kostinski and Shaw 2001; Pinsky and Khain 2003; Chun et al. 2005; Duncan et al. 2005; Bec et al. 2007; Lehmann et al. 2007; Ayala et al. 2008; Salazar et al. 2008; Saw et al. 2008; Siebert et al. 2010; Bateson and

---

[a] Current affiliation: SeeReal Technologies, Dresden, Germany.
[b] Current affiliation: Max Planck Institute for Dynamics and Self-Organization, Göttingen, Germany.

Corresponding author: Susanne Glienke, sglienke@mtu.edu

Aliseda 2012; Saw et al. 2012a,b; Ireland et al. 2016; Schmidt et al. 2017; Larsen et al. 2018). This paper represents another attempt to detect clustering at fine scales, but via the route of hypothesis testing. Our experimental strategy is conservative insofar as we pick the most homogeneous looking yet horizontally extensive and steady stratocumulus clouds as least likely to exhibit clustering. If droplets even in such mundane clouds do indeed cluster, current theories regarding droplet growth and radiative transfer should be suitably modified (e.g., Sundaram and Collins 1997; Cairns et al. 2000; Reade and Collins 2000; Kostinski 2001; Shaw et al. 2002; Devenish et al. 2012; Larsen and Clark 2014; Matsuda et al. 2014; Frankel et al. 2017).

Several methods of quantifying droplet clustering have been used (e.g., Baker 1992; Borrmann et al. 1993; Uhlig et al. 1998; Kostinski and Jameson 2000; Chaumat and Brenguier 2001; Pinsky and Khain 2001; Shaw et al. 2002; Marshak et al. 2005; Baker and Lawson 2010; Larsen 2012) but uncertainties are difficult to characterize, especially when using one-dimensional data ranging from millimeter to kilometer scales to infer three-dimensional spatial information (e.g., Holtzer and Collins 2002; Larsen 2012; Larsen et al. 2014). Higher-frequency one-dimensional instruments and therefore a possible resolution of ever-finer spatial scales, and hence smaller detection volumes, lead to decreasing droplet numbers and the associated uncertainties grow. Even when extended to three dimensions, such as with holographic instruments, averaging over multiple sample volumes is required because the particle pair correlations are modest and sampling noise is prevalent (Larsen et al. 2018). Therefore, the results of studies trying to quantify clustering become hard to judge. Here we focus on statistical significance of clustering, even if at the expense of quantifying clustering strength. To that end, we turn to hypothesis testing of the question: How certain are we that macroscopically homogeneous-looking, weakly turbulent stratocumulus are statistically homogeneous?

We use holographic data that provide the positions and sizes of droplets contained within single, localized sample volumes. To get at centimeter-scale variability, the hologram sample volume is sliced in various ways to test for population inequality of the resulting halves. Droplet position data are examined via cumulative distribution functions (CDFs) of counts. This way, binning associated with probability density functions (PDFs; or histograms) is avoided. To keep the interpretation parsimonious, we also avoid assuming any particular number distributions and keep the data processing nonparametric. For these reasons, the Kolmogorov–Smirnov test (Kolmogorov 1933) serves here as a primary statistical tool because it addresses a well-defined question: To what level of confidence do two given CDFs come from the same population? In other words, the null hypothesis is that the two CDFs are from the same population. The failure of the null hypothesis is then specified to some statistical level of significance. In our context, the fundamental question then becomes, Are the measured droplet counts per hologram (or, on a smaller scale, within a hologram) compatible with what one would expect for random spatial distributions, that is, statistical uniformity? We examine the data from three-dimensional in situ measurements of droplet numbers for the presence of droplet clustering in either hologram to hologram (outer scale) or between opposite halves of the same hologram (inner scale) count fluctuations. In this "minimalist" approach, we focus on just counting drops observed in different measurement volumes and using these counts to examine whether the droplet counts are consistent with an underlying homogeneous Poisson process (Poisson distribution at all spatial scales).

2. Description of the cloud particle data

The data were collected during the Cloud System Evolution in the Trades (CSET) field project from 1 July to 15 August 2015, which targeted marine stratocumulus and trade wind cumulus clouds over the Pacific Ocean between the coast of California and Hawaii. The measurements were conducted with a variety of instrumentation on board the NSF/National Center for Atmospheric Research (NCAR) Gulfstream-V High-Performance Instrumented Airborne Platform for Environmental Research (GV HIAPER) aircraft (Earth Observing Laboratory 2005). Further information on meteorological and cloud conditions during CSET is provided by Albrecht et al. (2019).

Conventional instruments for measuring cloud droplet size and spatial distributions, including those based on light scattering such as the cloud droplet probe (CDP) and light shadowing such as the two-dimensional optical array cloud probe (2DC), measure along the flight path with a small sample area cross section. Obtaining enough counts to estimate a size distribution requires relatively long sampling times, and therefore a very long and thin (essentially one-dimensional) sample volume. Thus, to examine droplet counts on finer spatial scales, for example, down to centimeters, holography offers an opportunity by supplying a spatially localized sample volume of order $10\,cm^3$ with a wide range of drop sizes and counts. For each hologram, a pulsed laser provides a snapshot of all droplet sizes and positions in a local sample volume by creating overlapping diffraction patterns from each droplet that can be reconstructed in
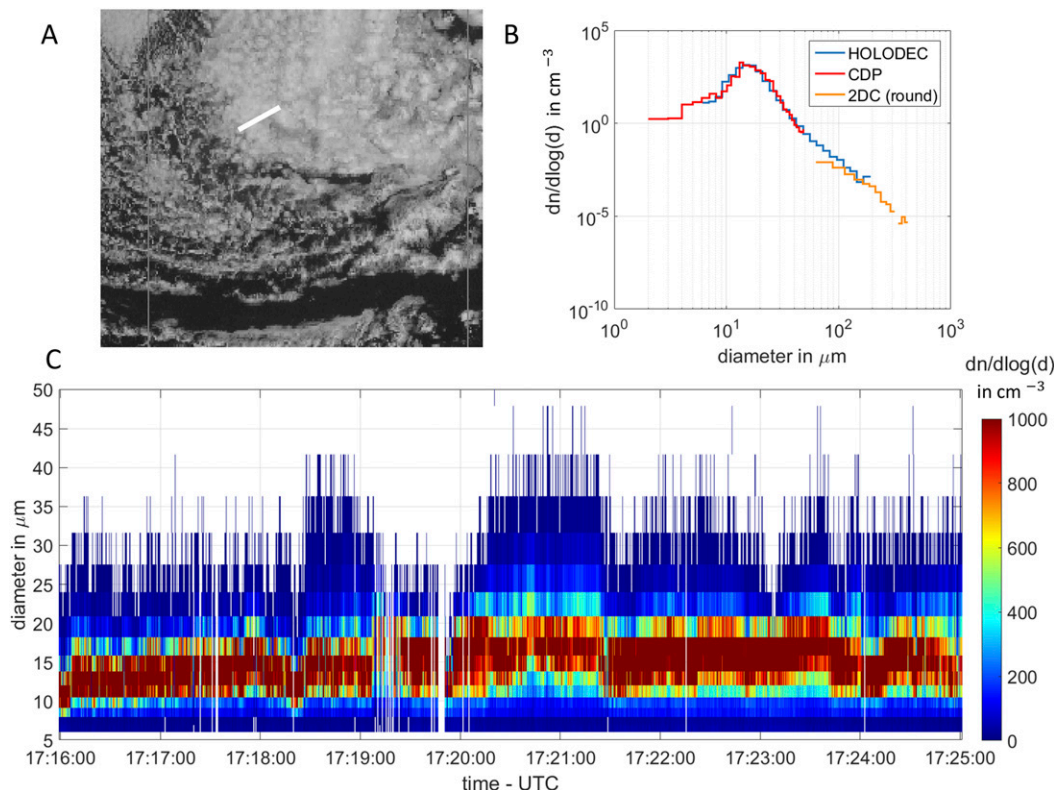
FIG. 1. Overview of properties of the cloud. (a) Satellite image at 1730 UTC, with the 75.4 km flight path indicated by the white line. (b) Size distribution measured by HOLODEC, CDP, and 2DC averaged over the entire length of the flight segment. (c) Changes along the flight path, with the aircraft altitude at the top and the size distribution change from hologram to hologram at the bottom. By using the axes as shown in (c), the changes are magnified and seem bigger than they are. It is evident that the cloud deck is continuous with only few breaks (the gap at 1719:50 UTC is missing data) and few changes over the 75.4 km flight path.

postprocessing (Fugal and Shaw 2009). Therefore, spatial scales within holograms can be examined, which are much smaller than those available for conventional cloud probes. During CSET, the Holographic Detector for Clouds (HOLODEC) was one of the instruments deployed, together with more conventional instruments (both CDP and 2DC) (Glienke et al. 2017). HOLODEC has a total sample volume of approximately 13 cm $\times$ 1 cm^2, of which we use a subvolume of 1.16 cm $\times$ 0.68 cm $\times$ 12.0 cm for this analysis, and can detect droplets with diameters of 6 μm up to millimeters with the best detectability above 10 μm (Fugal and Shaw 2009; Spuler and Fugal 2011). Holograms were sampled at 3.3 Hz corresponding to 40 m for the flight speed of 140 m s^{-1}. This sampling enables the examination of variability on intrahologram scales of about 5 cm as well as the longer interhologram scales of about 40 m. Intrahologram scales are determined by the longest dimension of each holographic sample volume, whereas the interhologram scale is determined by the camera frame rate and the flight speed.

Seeking steady, homogeneous conditions we chose a cloud segment with a constant flight altitude in an extended cloud layer, a rare occurrence in the CSET dataset. This occurred on flight RF02 on 7 July 2015 when the aircraft sampled a stratocumulus deck at a constant altitude of $\approx$1190 m between 1716 and 1725 UTC (36.87°–37.20°N, 136.2°–136.9°W) on its way to Hawaii. The cloud deck extended beyond the chosen time period, but both altitude changes as well as cloud edges are excluded here. These 9 min of cloud sampling represent 75.4 km of in-cloud data (1816 holograms in total) that visually appears continuous and reasonably homogeneous (see Fig. 1 and Fig. 2b). We include all droplets that are larger than 6 μm in diameter, with the largest measured drop being 162 μm.

Details about the examined cloud are shown in Fig. 1, where Fig. 1a shows the satellite picture of the region as well as the flight path in white. From this it is evident that the deck of clouds that was sampled at constant altitude was extensive and continuous with only a few gaps.
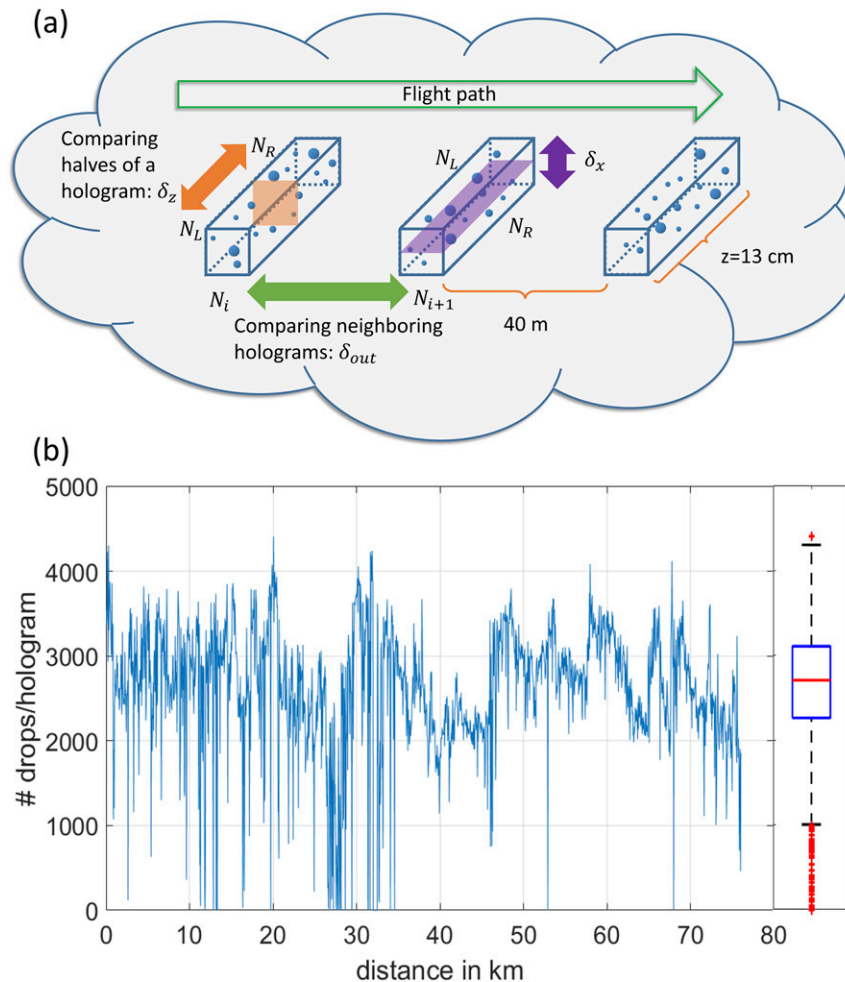
FIG. 2. (a) Schematic of HOLODEC data collection and analysis. To calculate $\delta_{\text{out}} = (N_i - N_{i+1})/\sqrt{N_i + N_{i+1}}$, consecutive holograms (~40 m apart) are compared pairwise. For $\delta_z = N_L - N_R/\sqrt{N_L + N_R}$, counts for the two halves of the same hologram (defined by the orange plane) are used; the same process holds for δ_x (defined by the purple plane) and for δ_y (not shown). (b) Droplet count per hologram vs distance. All holograms are of equal sample volume: $1.16\,\text{cm} \times 0.68\,\text{cm} \times 13.0\,\text{cm}$. The aircraft average speed of $138.5\,\text{m s}^{-1}$ yields an interhologram distance of 41.5 m and the total length of about 75.4 km. The box-and-whisker plot on the right side denotes mean count (2623; orange line), the 25th and 75th percentiles (2262 and 3107, respectively; blue box), and the 0.35th and 99.65th percentiles (whiskers).

The size distribution along the flight path (Fig. 1c) does not vary a lot, so the averaged size distribution (Fig. 1b) can be seen as representative of the whole cloud. For a marine environment the mode diameter at about $15\,\mu\text{m}$ indicates relatively small but numerous droplets, but a few large drops can also be found.

3. Data processing

a. Choice of random variable to test outer- and inner-scale uniformity

Statistical homogeneity of droplet counts N depends on spatial scale; for example, visual inspection of Fig. 2b leads to readily discernible local trends in concentration. The average number of droplets in a hologram and the corresponding standard deviation are 2623 ± 743, whereas a Poisson distribution with the same mean would only have a standard deviation of 51 droplets. Thus, the cloud droplet numbers do not follow a homogeneous Poisson distribution over the 75.4 km scale associated with the entire flight interval. Furthermore, there are inhomogeneities on scales of at least 40 m and up, but what about much smaller spatial scales? Are they ever so distributed when the concentration appears quite steady over some smaller subsegments? In this section we construct a random variable δ that will allow

us to use the Kolmogorov–Smirnov (K-S) test at a sub–hologram scale.

To apply the (one-sample) K-S test, the empirically observed CDF of some variable is compared to the theoretical CDF proposed to describe the data. The absolute maximum of the difference is used to judge the likelihood that the empirical data come from the theoretical CDF (see p. 476 of Kendall and Stuart 1979).

To that end, let the number of cloud drops in sample volume A be N_A and in sample volume B be N_B, with A and B being two neighboring volumes such as two neighboring halves of an individual hologram. The measured distribution of $\Delta_{AB} = N_A - N_B$ can then be compared to one drawn from two identical Poisson distributions (the perfectly random case). In passing, we note that the difference between the two Poisson-distributed random variables follows the Skellam distribution (Skellam 1946). In the absence of clustering, the two Poisson variables have the same mean, yielding for the distribution of the difference mean and skewness of zero and variance of 2μ (where μ is the mean for each of the Poisson-distributed random variables N_A and N_B). Hence, we introduce the random variable δ:

$$\delta = \frac{\Delta_{AB}}{\sqrt{2\mu}} = \frac{N_A - N_B}{\sqrt{N_A + N_B}}, \tag{1}$$

where for real data the sample mean $\mu = (N_A + N_B)/2$ is used in place of the true mean.

The δ approach can be applied at any spatial scale. For example, exploring homogeneity on 40 m scales, involves droplet counts in consecutive holograms: N_i and N_{i+1}. In Eq. (1) we therefore use N_i and N_{i+1} for N_A and N_B, respectively, thereby allowing us to compute a quantity we call δ_{out} (for "outer scale" variability).

The δ metric is crucial at subhologram scales where uniformity within a single hologram is in question. In this case, A and B are two halves of one hologram and the quantity examined is the difference in their droplet counts. Two possible ways of partitioning a hologram in halves are illustrated in Fig. 2a. A three-dimensional Cartesian coordinate system can be aligned parallel to the symmetry axes of the holographic sample volume, with the shorter dimensions running parallel to the x and y axes, and the long axis running along the z direction, centered at the origin. To explore the subhologram scales, we replace A and B in Eq. (1) with L and R with N_L corresponding to the number of drops with $z > 0$ ($x > 0$) and N_R corresponding to the number of drops with $z < 0$ ($x < 0$) to define δ_z (δ_x). Thus, in the left picture in Fig. 2a, we have marked the orange-square as dividing the hologram along the plane $z = 0$. Similarly, the center picture shows the same hologram divided in
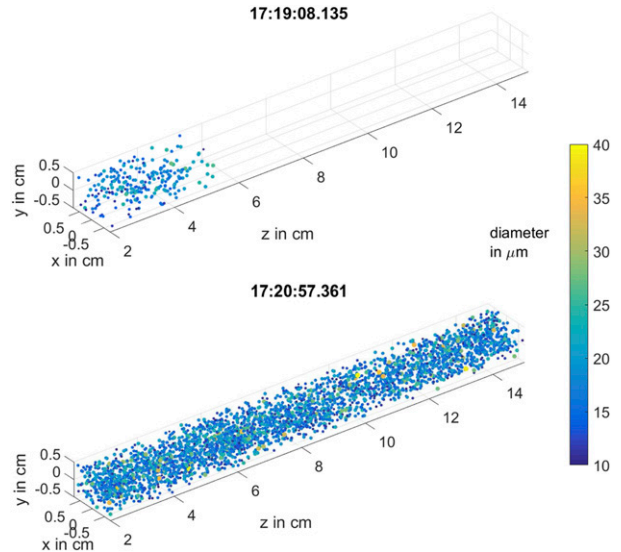

FIG. 3. Two examples of holograms showing very different conditions of droplet distributions. Both holograms have similar values for ΔN (131 and 151), but due to the different total numbers (top) $N_1 = 131$ and (bottom) $N_2 = 2041$, the values for δ are very different (11.4 and 3.3). Furthermore, it is evident that cloud edges were sampled during the flight, although this is the only hologram from all 1816 examined holograms with no cloud droplets in one-half.

half by the purple rectangle along the plane $x = 0$. Additionally, it is also possible to slice the hologram in half along the plane $y = 0$, yielding δ_y.

Because there is a gradual decrease in instrumental sensitivity with increasing z (Fugal and Shaw 2009), the division point for δ_z was moved slightly closer to the image plane than the center of the sample volume, so that—when averaging over all holograms in the flight interval—all detected particles were equally likely to be found in either half of the hologram. For the specific flight examined here, this meant moving the dividing surface defining δ_z about 5 mm closer to the image plane of the hologram to ensure this equal probability (compared to the total length of 120 mm along the z dimension). The dividing surface placement was determined from the data, and may therefore change if a different droplet size range or a different dataset are considered. Similarly, the dividing planes for the x and y directions were shifted by 0.12 and 0.02 mm, respectively, compared to a total dimension of about 1 cm.

The importance of measuring droplet count differences in units of standard deviations δ is illustrated in Fig. 3. The top panel shows a hologram with one-half empty (a remarkably sharp cloud edge). The total number of droplets is 131. In contrast, the bottom hologram contains droplets seemingly uniformly distributed throughout the entire sample volume, 2041 in total.

The droplet count difference between the two halves is $\Delta_{AB} = 151$, similar to the difference in the top hologram $\Delta_{AB} = 131$. However, one hologram shows a clear nonuniformity in droplet positions whereas the other does not, as seen at once in terms of δ: the top hologram $\delta = 131/\sqrt{131} = 11.4$ versus the bottom hologram value of $\delta = 151/\sqrt{2041} = 3.3$. Note that the top hologram in Fig. 3 is the sole example from the 1816 holograms with an empty half.

Once the empirical distributions of δ_{out}, δ_z, δ_x, and δ_y are obtained from the data, the analysis inspired by the K-S test can be applied to determine whether these empirical distributions are consistent with perfect randomness. The one-sample K-S test requires comparison to a theoretical δ distribution, which is discussed next.

b. Monte Carlo simulations supply the reference for the K-S test

Ideally, one would prefer to use a theoretical reference for the one-sample K-S test. However, the local mean is a random variable itself as it varies unpredictably from hologram to hologram. At first glance, the Skellam variable, scaled as in Eq. (1), appears attractive because its first three moments are independent of $\mu = (N_A + N_B)/2$. However, the kurtosis does have a weak μ dependence. More importantly, the cumulative distribution of $N_A - N_B$, scaled by $(2\mu)^{1/2}$, still displays a subtle μ dependence via the variable step height as illustrated in Fig. 4. Therefore, we resort to binomial Monte Carlo trials to supply the unclustered reference, denoted δ_{mc}, to compare to the measured δ_{out}, δ_z, δ_x, and δ_y as discussed next.

To compute δ_{mc}, the total observed number of droplets in two neighboring holographic volumes is randomly redistributed so that the two volumes still contain the same total number of droplets, but each droplet has an equal probability of being assigned to each volume (e.g., left half vs right half of the simulated hologram). In other words, Bernoulli trials for the binomial distribution with $p = 1/2$ and n equal to the total number of droplets in each hologram. Then the redistributed synthetic data are used to generate a distribution of δ_{mc} values for a full "flight" of 1816 holograms. This process was repeated a total of 1000 times, so that there are 1000 synthetic datasets as well as the one observational dataset. This number seems large enough, since the total spread of δ_{mc} does not increase appreciably if 10^5 datasets are generated. Several refinements to the Monte Carlo simulations are described in section 5.

The method for obtaining the simulated results allows for gradual changes in droplet counts over multiple holograms but locally—within single holograms—explicitly forces perfect spatial randomness. Based on this, δ_{mc} is
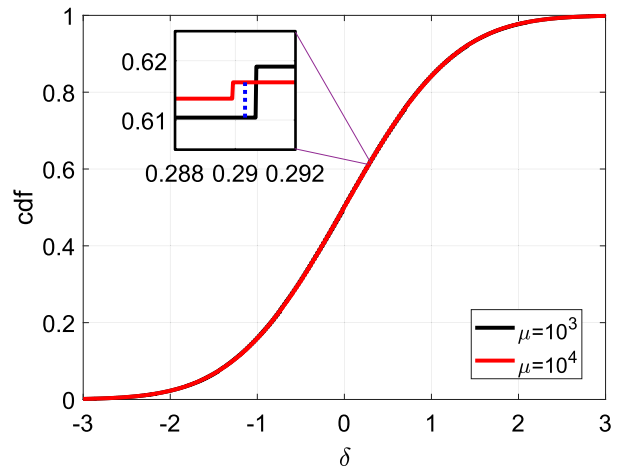

FIG. 4. A comparison between CDFs of the Skellam variable, scaled as in Eq. (1). Each curve comes from the numerical simulation of 10^6 differences between pairs of Poisson distributions; the black curve shows the CDF of $(N_A - N_B)/\sqrt{2\mu_1}$, with $\overline{N_A} = \overline{N_B} = \mu_1 = 10^3$, and the red curve shows the CDF of $(N_A - N_B)/\sqrt{2\mu_2}$, with $\overline{N_A} = \overline{N_B} = \mu_2 = 10^4$. Despite seemingly excellent agreement, the fundamental discreteness of the distributions due to $\mu < \infty$ (see inset staircase) causes the Kolmogorov–Smirnov test to detect that these two CDFs do not result from the same underlying probability distribution.

the distribution of δ expected if the data were consistent with this local spatial randomness. In the following, the simulated δ_{mc} will be compared to the measured values of δ, to decide via the K-S test whether the observations are consistent with the randomness hypothesis at spatial scales of $\sim$40 m (δ_{out}), $\sim$5 cm (δ_z), and $\sim$0.5 cm (δ_x and δ_y).

This test compares two distributions based on the maximum absolute difference h between the respective CDFs. The distribution of h_{mc} obtained via Monte Carlo is used to determine the likelihood and thereby statistical significance of the observed h. Large h would then indicate statistically significant deviations from perfect randomness. Note that the magnitude of h is, in this framework, a measure of statistical significance rather than the strength of droplet clustering.

4. Results

a. Statistical significance of the evidence for droplet clustering

Droplet counts per hologram are shown in Fig. 2b, with the interhologram distance of about 40 m. A total of 1816 holograms were collected along the 75.4 km of flight path, with observed droplet counts between 0 and 4410, and the global average of 2623 $\pm$ 743 (standard deviation). As expected for a random count (nonnegative random variable), the excursions below the mean are more frequent than those above.
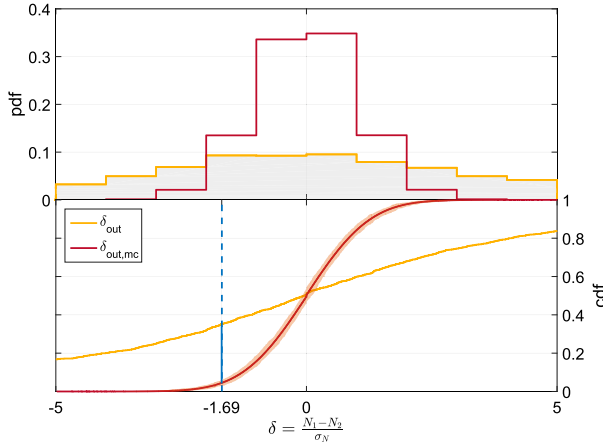
FIG. 5. (top) PDFs and (bottom) CDFs for observed interhologram δ_{out} (see Fig. 2) for all droplets >10 μm (orange line with gray shading below) vs the fiducial uniform Monte Carlo (red line), simulating the experiment. The range of observed values of δ_{out} on this 40 m scale far exceeds the range for the uniform $\delta_{out,mc}$ in the top panel, thereby detecting nonuniformities with statistical significance. The dashed blue line in the bottom panel marks $\delta = -1.69$, where the maximum K-S distance h (solid line) occurs. At $\delta = -1.69$ the respective values for the cumulative probabilities are 0.05 and 0.35. Thus, the K-S test rejects the null hypothesis of a single underlying distribution with compelling confidence.

Is the hologram to hologram variability on 40 m scales seen in Fig. 2 comparable to expectations for spatial homogeneity? To that end, δ_{out} is compared to $\delta_{out,mc}$ generated from the Monte Carlo simulation of the same experimental conditions, as described in section 3b. Figure 5 shows the two distributions obtained for δ_{out} and $\delta_{out,mc}$ both as PDFs (top panel) and CDFs (bottom panel). The envelope of $\delta_{out,mc}$ CDFs is also shown by the light-red shading in the bottom panel so that the range of variability in the Monte Carlo trials can be appreciated. It is obvious from the plot that the distributions for δ_{out} and $\delta_{out,mc}$ are far apart. The wider PDF of the observations compared to the reference simulation signifies larger variability at this scale than random fluctuations can explain. The range for the measured δ_{out} is −75 to 72, whereas $\delta_{out,mc}$ approaches zero probability for $|\delta|$ values of greater than 5. The largest distance between the two CDFs, the maximum K-S distance h, occurs at the vertical blue dashed line and indicates a difference in probability of 0.3—vastly larger than the spread of the 1000 Monte Carlo realizations. This shows that hologram droplet count fluctuations are much more pronounced than random fluctuations at the ≈40 m scale.

Coming to our central result, we now consider intra-hologram variability (centimeter scale). Figure 6 shows the distributions of the mean Monte Carlo $\delta_{z,mc}$ (dark green line) and the observed δ_z. There are apparent
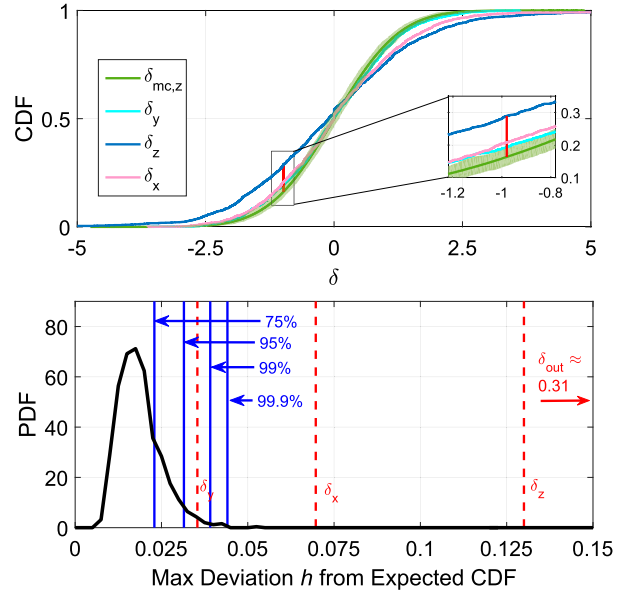

FIG. 6. (top) Observed CDF for δ_z (black) and an envelope of 1000 simulated statistically uniform CDFs and their mean (green). The CDF of the observations is clearly outside the envelope of the simulations. The inset zooms in on the maximum distance between δ_z and the mean of Monte Carlo CDFs. (bottom) The black curve is a histogram of the largest difference between trials and the expected value of δ_{mc}. Blue vertical lines mark empirical uncertainty: 990 of the 1000 Monte Carlo trials had a maximum deviation from the mean CDF < 0.04, yielding a 99% confidence bound. Only δ_y lies within this confidence bound. Thus, centimeter-scale CDFs of neither δ_z nor δ_x are compatible with the null hypothesis of statistical uniformity to 99.9% statistical significance. The same is true for δ_y, but only to 95% statistical significance.

differences, with the measured distributions of all δ broader than the Monte Carlo (Fig. 6, top panel). To see whether these differences are outside the sampling variability (spread), we include the envelope of the extremes of the 1000 Monte Carlo simulations (light-green shading in the top panel of Fig. 6). The observations are still outside the envelope of the Monte Carlo simulations.

In accordance with the K-S test, but supplying the measure of significance directly from the Monte Carlo results, we compile a histogram of h_{mc} for each of the 1000 Monte Carlo trials compared to the CDF of the average Monte Carlo result. As shown in the bottom panel of Fig. 6, the histogram serves as an empirical estimate of confidence bounds: the bounds for 75%, 95%, 99%, and 99.9% significance are shown by vertical blue lines. The maximum difference h between the δ_z CDF and the mean Monte Carlo CDF is marked by the vertical red dashed line at $\delta_z = 0.13$. Therefore, one concludes with some confidence that the droplets cluster at the local-hologram ≈5 cm scale.

Figure 6 also shows the CDFs and maximum deviations h from Monte Carlo for δ_x and δ_y. These correspond to slicing the volume along x and y planes, and therefore bring the minimum scale down to ≈ 5 mm. The CDFs for both δ_x and δ_y are just outside the envelope of Monte Carlo results (see inset). Nonuniformity within the x-sliced registers well beyond the 99.9% level (Fig. 6, bottom panel), whereas within the y-sliced volumes is between the 95% and 99% confidence levels and is therefore less certain. Thus, although unlikely, the shape of the δ_y CDF could be explained by random fluctuations of droplet numbers.

Before concluding that clustering is real, however, we must further examine all plausible instrumental sources of variances that might even slightly alter the shape of the Monte Carlo CDF, and therefore the K-S distance h. Also, the variance of the distribution of h_{mc} in the bottom panel of Fig. 6 may increase. Either effect might decrease the significance that clustering is detected. To eliminate the latter possibility, we thoroughly explore different approaches for accounting for known instrumental biases such as edge effects, position biases and changing detection probability within the sample volume, even with respect to different size ranges. These do not drastically alter our conclusions, but for completeness are described in section 5.

b. Significance of clustering and droplet size

Thus far we have examined droplet spatial variability independent of the sizes of individual droplets. However, there are reasons to suspect differences in variability for various droplet size ranges. For example, finite particle inertia, gravitational settling and turbulence effects can lead to spatial correlations (Reade and Collins 2000; Bec et al. 2007; Saw et al. 2008, 2012b; Bec et al. 2014; Gustavsson et al. 2014; Ireland et al. 2016). Thus, we extend our analysis to examine the significance of clustering in different size ranges.

The analysis proceeds as before, that is, the sample volume is divided into two halves to calculate a value for δ, but this time for four different size ranges, 6–12.5, 12.5–14.6, 14.6–16.4, and $>16.4\,\mu$m. The size ranges were chosen such that the number of droplets in each of the four intervals was constant; that is, one-fourth of all droplets were in each size range. This allows us to use one rescaled Monte Carlo experiment for determining (N dependent) significance. For each size range we divide the sample volume such that the median of δ_z equals 0 when averaging over the 1816 holograms. This shifts the dividing plane (colored orange in Fig. 2) by at most 3 mm in each direction. Then for each hologram a value of δ was calculated and compared to the Monte Carlo simulation as before.
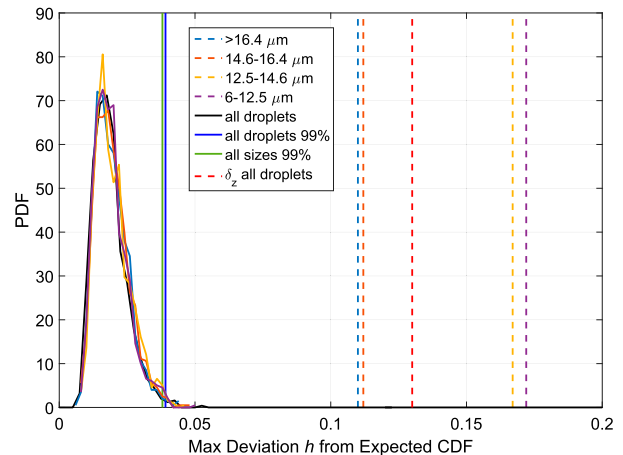

FIG. 7. Shown are five PDFs of h_{mc} as indicated by the droplet diameter ranges in the legend. The black PDF is the same as that shown in Fig. 6. The blue, red, yellow, and purple vertical lines mark the observed h of the four diameter categories. Data are for the z partition of the hologram, i.e., δ_z. The green vertical line delineates the range of 99% significance for each of the four size ranges, and the solid blue line is the 99% confidence bound from Fig. 6. Statistical significance is compelling in all four cases individually but is observed to decrease with increasing droplet diameter.

Figure 7 shows the maximum absolute distances between the CDFs of δ_z and $\delta_{z,\mathrm{mc}}$ for each of the four size ranges. The maximum observed deviations h decrease with increasing droplet size, which indicates increasing confidence toward the null hypothesis of perfect randomness. This indicates lower confidence for clustering for larger droplets. However, when examining all four deviations individually to their associated Monte Carlo distributions of h_{mc} the figure still shows clustering with compelling confidence. Observe that larger particles show lower h than smaller particles.

One can see from Figs. 6 and 7 the crucial element in rejecting the null hypothesis of perfect randomness is the shape and envelope of Monte Carlo CDFs (of δ_{mc}). These yield both the magnitude of h and the width of the Monte Carlo distribution of h_{mc}. Should this latter distribution broaden and in particular develop a fatter right tail, the statistical significance can drop drastically. From a different perspective, the Poisson test of perfect randomness (variance equal to mean count) can produce spurious results because of unaccounted sources of variance. This emphasis on the fidelity of such fiduciary use of Monte Carlo simulations prompted us to examine the measurement process more closely in the next section.

5. Possible instrumental sources of variance

Are there unidentified sources of variance in the instrument or sampling strategy that would cause reduced

confidence in the significance testing for homogeneity? Here we describe our attempts to account for instrumental imperfections that could manifest as apparent clustering. To that end, we incorporate possibly hidden sources of instrumental variability into more sophisticated MC simulations, described next. Additional tests such as detected nonzero skewness in the distributions of Δ, are also described and confidence bounds scrutinized.

a. Enhanced Monte Carlo simulations

Our explicit goal here is to simulate the measurement process faithfully. Each of the simulations had some general properties in common:

- Simulations draw from counts of the 1816 holograms, in order to most closely match the dataset being analyzed (except the last method, which considers additional droplet position information from the full research flight).
- Simulations have the same hologram-to-hologram sampling variability: the ith hologram in the simulation contains exactly as many cloud droplets as the ith hologram in the data.
- Simulations place droplets within the same 1.16 cm $\times$ 0.68 cm $\times$ 12.0 cm parallelepiped of the HOLODEC sample volume.
- Simulations involved halving the hologram along x–y, x–z, and/or y–z planes to allow for the computation of Δ_z and δ_z, Δ_y and δ_y, and Δ_x, and δ_x, respectively.

The simplest simulation, described in section 3b, placed particles in the appropriate octant perfectly randomly; a numerical "coin flip" assigned each particle into high or low x values, high or low y values, and high or low z values independently and with equal probability. After completing this simulation for 1000 simulated flights, the observed distributions of Δ_x, Δ_y, Δ_z, δ_x, δ_y, and δ_z were compared to the simulated values.

When these simulations failed to show similar distribution functions for δ and Δ as the observed data, attempts were made to incorporate more realistic boundary conditions, such as various shapes for the sample volume and dividing lines between the two "halves" of the hologram. As part of the analysis described in section 2, the dividing plane has been shifted by distances on the order of millimeters from the physical midpoint of the sample volume, to the location resulting in equal probability of detecting the same number of droplets in both halves. Careful scrutiny reveals that for holograms with very different droplet numbers, this median droplet count position varies; that is, if we only examine the holograms with lower or higher than average droplet numbers, the dividing plane is slightly to one side or the other of the average dividing plane. To check how this might influence the conclusions, we ran a set of Monte Carlo simulations in which holograms with low droplet numbers were calculated with a higher probability of finding droplets within the first half than holograms containing high droplet numbers. This, of course, influences the results for the calculated $\delta_{z,\mathrm{mc}}$ but causes minimal changes to the distribution of h_{mc} and does not account for differences between the observations and the Monte Carlo results.

In attempt to account for the possible corrupting influence of variable instrument sensitivity (meaning that the volume has regions in which droplets are detected with slightly higher or lower probability) another simulation method was developed. In this method (which we have dubbed the "enhanced Monte Carlo") the 4 763 670 recorded droplet positions within the sample volume make up a "library" of locations. Simulations then draw from this library to place cloud droplets in each hologram. For each hologram in each of 600 simulated flights, the observed number of cloud droplets were placed by randomly selecting the necessary number of these 4 763 670 locations. Then, holograms were again sliced into halves and distributions of Δ_x, Δ_y, Δ_z, δ_x, δ_y, and δ_z were compared with the measured observations. As can be seen in Fig. 8, there is little change in moving from an idealized perfectly random Monte Carlo simulation to this "enhanced" Monte Carlo.

To push further, we used the measured droplet positions recorded in the full research flight as a library with 14 802 holograms (i.e., from more than just the 1816 holograms used in this paper), from which the droplets for the simulation are randomly drawn. This method accounts for locations in the holograms where droplets are more frequently detected than the ideal assumption of uniform detection probability. Clustering and irregularities due to these highly populated areas are thereby included in the Monte Carlo simulation. As before, each simulated hologram has the same number of droplets as the real measured hologram. The flight segment of RF02 containing 1816 holograms is simulated 600 times (fewer than the 1000 used in section 3 due to computational expense, but still adequate for smooth Monte Carlo distributions). Similar to the observations, the location of the dividing line for the calculation of δ is determined in such a way that half of all droplets, averaged over the 1816 holograms, are in each half of the hologram. From this simulation, values for δ can be determined and thus a distribution for each realization of the flight segment. Still, the comparison between the simplest and the most detailed Monte Carlo simulations shows that they yield very similar results; the obtained distributions of
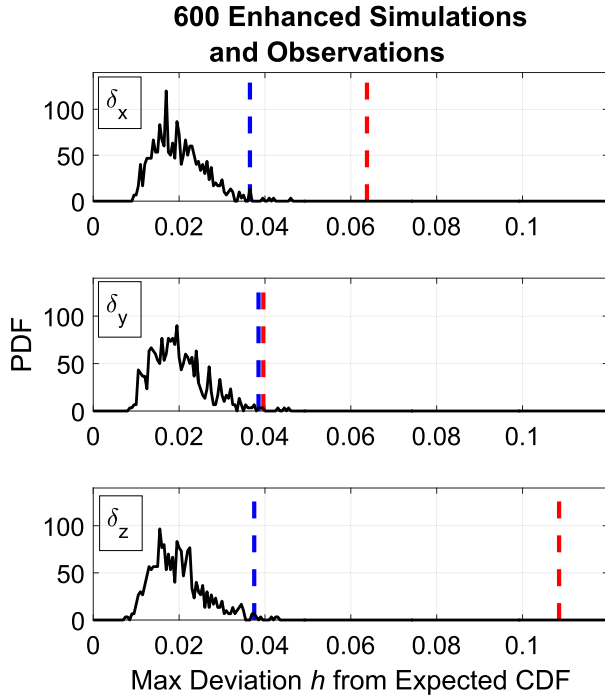
FIG. 8. As in Fig. 6, (bottom) but accounting for slight inhomogeneities in instrument detection probability. This shows the largest difference between the simulated (black) and observed (dashed red vertical line) CDFs of δ and the average CDF of δ among the 600 simulated flights using the "enhanced Monte Carlo" simulation as described in section 5. The dashed blue lines show the 99th-percentile significance obtained from the Monte Carlo simulations. The figure shows results for (top) δ_x, (middle) δ_y, and (bottom) δ_z, with each histogram corresponding to 600 enhanced Monte Carlo simulations. The observed h exceeds the 99th percentile for all three partitions, therefore implying statistically significant clustering.

FIG. 9. Removal of holograms with a large $|N_L - N_R|$ for the x dimension illustrated. These are exclusively holograms influenced by shattered rain. (top) Histogram of the difference in number of droplets in each half for x dimension. Holograms with $N_L - N_R < -200$ are marked as outliers. (bottom) CDFs of δ_x for all holograms and when outliers are removed for both the observations and the Monte Carlo simulation. The two simulations are very close to each other. The inset shows the differences more clearly.

δ are so close that they are barely distinguishable. The largest distance h between two CDFs is 0.01, which is comparable to the smallest values for h between different Monte Carlo trials of one simulation.

b. Skewness in droplet counts

The measurement process can be imperfect in ways not affecting variance but symmetry instead. For example, the right half of a hologram is just as "good" as the left, requiring that the skewness of the $\Delta_{LR} = N_L - N_R$ distribution should be zero to within tolerance. So it was with concern that we noticed a skewness in Δ distributions for both x and z of -1.1 and 0.6, respectively, much greater than 0.2 the maximum skewness in the Monte Carlo simulations (but y is within MC bounds, all for 1000 realizations). What is the source of this skewness, and would removing the source make the clustering disappear? To that end, we looked at each of the 1816 holograms individually and discovered that just a few
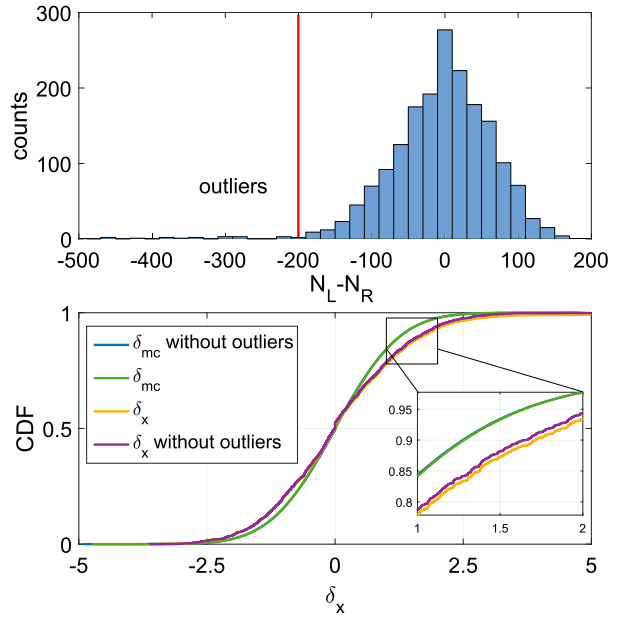
contribute disproportionately to skewness. These turn out to be contaminated by rare, shattered drizzle drops: in such holograms chains of drop fragments appear on one side of the hologram sample volume, close to the instrument housing. They are the outliers in the left tail of the histogram of $\Delta = N_L - N_R$ shown in the top panel of Fig. 9. The x-partition data are shown because it has the largest magnitude of skewness. Recall that the x dimension is perpendicular to the flight direction, partitioning the hologram into top and bottom halves (cf. top panel of Fig. 2). All holograms with $|\Delta| > 200$, present exclusively in the left tail of the histogram in the top panel of Fig. 9 have been identified as including shattering events. Conversely, no obvious shattering events have been found in the remaining (vast majority) holograms. The 18 culprit holograms do not occur randomly but rather nearly consecutively, next to a burst of empty holograms in a cloud hole. A few occur new the very beginning and end of the time series (cloud edges). Exclusively negative Δ for all culprit holograms implies that shattering events occur exclusively in the bottom half of the hologram, probably due to a lack of top–bottom symmetry in the flow pattern.

Before removal of the 18 holograms, the average skewness of the Δ_x distribution is -1.1 and after the

removal it is -0.19, within the 0.2 range of sampling variability for the 1000 Monte Carlo realizations. Do these rare shattering events affect our clustering conclusions? The bottom panel of Fig. 9 shows that when we remove these outlier holograms the shape of the CDF changes slightly but perceptibly. How does this shift toward the Monte Carlo CDF affect the K-S distance h and the associated level of significance? Figure 10 answers the question, showing the shift of h for δ_x, δ_y, and δ_z toward lower but still compelling significance. As mentioned, the bars in Fig. 10 shift to the left because of the slight change in CDF shape toward MC, upon removal of the outliers. As an alternative to outlier removal, we could leave the data as is and incorporate drop shattering events into the Monte Carlo simulation itself, for example, via doubly stochastic Poisson process as illustrated for instance in Fig. 1 of Kostinski and Jameson (2000). This would indeed produce an extravariance due to the shattering-caused apparent clustering as such spatial correlations are "diluted" in our current ensemble Monte Carlo. However, the observed probability of (rare) shattering is subject to huge sampling variability, so our conservative ($|\Delta_x| > 200$) removal of outliers was deemed more reliable. Thus, the null hypothesis of no clustering is again rejected.

After the removal of the 18 holograms that had identified shattering events, the two CDFs for x and y still show differences despite their similar dimensions. This could be due to further shattering, since our removal was rather conservative. However, it is reasonable to consider y as free from shattering due to its different orientation. Still, y shows hints of clustering.

6. Concluding remarks

Recently, scale-dependent cloud droplet clustering in homogeneous stratocumulus clouds was detected using the three-dimensional spatial statistics of cloud droplet positions measured with a holographic instrument (Larsen et al. 2018). The emphasis there was on scale dependence, using the radial distribution function (3D version of pair correlation function). In contrast, in this paper we are not concerned with continuous scale dependence but instead focus on a statistical significance of clustering at a fixed (intrahologram) scale. To that end, we employ the Kolmogorov–Smirnov test because of minimal processing and manipulation of the data (droplet counts). In particular, no data binning is required (cumulative distributions are used) and the significance test is invariant with respect to the underlying distribution. Data analysis is exceedingly simple as well: each hologram volume is halved and droplet counts for
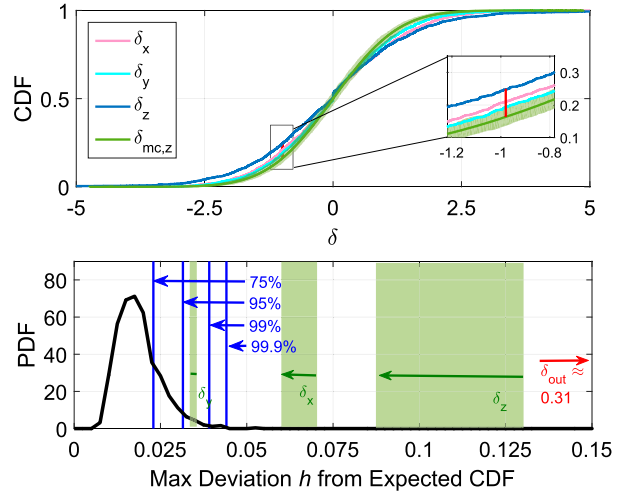

FIG. 10. Removing holograms with a high difference in $N_R - N_L$ for the x dimension, i.e., holograms influenced by shattered rain, reduces the maximum distances for all three dimensions. Nevertheless, the results indicate that the variability is still larger than expected for randomness for both x and z. (top) Observed CDF for δ_z (black) and 1000 simulated statistically uniform CDFs without outlier holograms. (bottom) Maximum deviations from the mean CDF for the Monte Carlo trials, their confidence bounds, and the observations. The green shading indicates the shift when outliers are removed; in all cases this will bring the observations in closer agreement with the Monte Carlo trials.

the two partitions are compared. Not much else is involved. Another virtue of this approach is how it exposes instrumental imperfections. We have partitioned sample volumes along the x, y, and z directions; and divided by droplet size; ultimately, we find that no matter which way we slice the data, the null hypothesis of perfect randomness in spatial distributions of droplets is rejected with compelling confidence. This complements the findings of the earlier study (Larsen et al. 2018).

How localized is the clustering detected by the K-S test used in this paper? Specifically, is it possible that large-scale gradients could contribute to the centimeter-scale K-S signature? Taking the perspective that fluctuations are deterministic spatial gradients, we can ask, do 40 m spatial gradients affect clustering on centimeter scale quantitatively? To that end, to be conservative, we pick the largest change of counts present in our data: 0–4000 within the span of 40 m. This is roughly 100 droplets per meter or 1 droplet per centimeter. The observed number fluctuations on centimeter scale as well as Poisson fluctuations both far exceed this. We, therefore, conclude, that the existence of gradients on the 40 m scale negligibly affect either the presence or absence of clustering. Conversely, we can ask: at what spatial scales would a 0–4000 fluctuation cause Poisson-comparable count fluctuations on the centimeter scale?

Assuming the standard deviation scales as the mean count, and using the Poisson square root rule, yields $\sim 60\,cm$, thus confirming our conclusion that the K-S method is reasonably localized in scale sensitivity.

Statistically significant clustering at centimeter scales (δ_z, δ_x, and δ_y) is consistent with turbulent mixing in marine stratocumulus clouds. However, in contrast with the length scale of $\sim 1\,cm$ and below in Larsen et al. (2018), the present $\sim 5\,cm$ scale is not likely to involve droplet inertia as a cause of clustering because the turbulent energy dissipation rates are typically rather low in such clouds. Clustering from entrainment and subsequent mixing of clear and cloudy air is the more likely cause.

Of course, statistical hypothesis testing never proves a particular physical mechanism, but rather rejects a null hypothesis with some confidence. Therefore, it is impossible to rule out the possibility that there is some unidentified instrumental source of variance not captured in the simulations, that artificially generates the observed difference between measured and simulated δ and that is *not* due to natural inhomogeneity in particle spatial distribution. This is in keeping with the "Anna Karenina principle" of statistics, that in hypothesis testing there are many ways the null hypothesis can be rejected (e.g., due to various natural or instrument-induced causes), but only one way it can be satisfied. Based on our analysis, and accounting for all plausible instrumental imperfections, we conclude that clustering on centimeter scales is indeed present. It is worth noting that the approach presented here can also be used for detection of instrumental imperfections such as spatially variable detection probability throughout the sample volume and other artifacts. For example, during application of the described test we found a nonuniform detection of droplets throughout the sample volume but this turned out to be negligible.

Finally, an investigation of size dependence shows that there is higher confidence for clustering of progressively smaller droplets. This intriguing result may have implications for our understanding of spatial clustering mechanisms. For example, theory and laboratory measurements suggest that nonsettling droplets in turbulent flow tend to become more clustered with increasing particle size (for Stokes numbers less than unity), but when gravitational settling effects become significant, the trends can be reversed (Bec et al. 2014; Gustavsson et al. 2014; Ireland et al. 2016). Indeed, for the droplet sizes considered here, and the weak turbulence conditions that prevail in stratocumulus clouds, it is likely that particles are in the sedimentation-dominated regime (Siebert et al. 2010, 2015).

REFERENCES

Albrecht, B., and Coauthors, 2019: Cloud System Evolution in the Trades (CSET): Following the evolution of boundary layer cloud systems with the NSF/NCAR GV. *Bull. Amer. Meteor. Soc.*, **100**, 93–121, https://doi.org/10.1175/BAMS-D-17-0180.1.

Ayala, O., B. Rosa, L.-P. Wang, and W. Grabowski, 2008: Effects of turbulence on the geometric collision rate of sedimenting droplets. Part I: Results from direct numerical simulation. *New J. Phys.*, **10**, 075015, https://doi.org/10.1088/1367-2630/10/7/075015.

Baker, B., 1992: Turbulent entrainment and mixing in clouds: A new observational approach. *J. Atmos. Sci.*, **49**, 387–404, https://doi.org/10.1175/1520-0469(1992)049<0387:TEAMIC>2.0.CO;2.

——, and R. P. Lawson, 2010: Analysis of tools used to quantify droplet clustering in clouds. *J. Atmos. Sci.*, **67**, 3355–3367, https://doi.org/10.1175/2010JAS3409.1.

Bateson, C., and A. Aliseda, 2012: Wind tunnel measurements of the preferential concentration of inertial droplets in homogenous isotropic turbulence. *Exp. Fluids*, **52**, 1373–1387, https://doi.org/10.1007/s00348-011-1252-6.

Bec, J., L. Biferale, M. Cencini, A. Lanotte, S. Musacchio, and F. Toschi, 2007: Heavy particle concentration in turbulence at dissipative and inertial scales. *Phys. Rev. Lett.*, **98**, 084502, https://doi.org/10.1103/physrevlett.98.084502.

——, H. Homann, and S. S. Ray, 2014: Gravity-driven enhancement of heavy particle clustering in turbulent flow. *Phys. Rev. Lett.*, **112**, 184501, https://doi.org/10.1103/physrevlett.112.184501.

Borrmann, S., R. Jaenicke, and P. Neumann, 1993: On spatial distributions and inter-droplet distances measured in stratus clouds with in-line holography. *Atmos. Res.*, **29**, 229–245, https://doi.org/10.1016/0169-8095(93)90005-9.

Cairns, B., A. Lacis, and B. Carlson, 2000: Absorption within inhomogeneous clouds and its parameterization in general circulation models. *J. Atmos. Sci.*, **57**, 700–714, https://doi.org/10.1175/1520-0469(2000)057<0700:AWICAI>2.0.CO;2.

Chaumat, L., and J. Brenguier, 2001: Droplet spectra broadening in cumulus clouds. Part II: Microscale droplet concentration inhomogeneities. *J. Atmos. Sci.*, **58**, 642–654, https://doi.org/10.1175/1520-0469(2001)058<0642:DSBICC>2.0.CO;2.

Chun, J., D. Koch, S. Rani, A. Ahluwalia, and L. Collins, 2005: Clustering of aerosol particles in isotropic turbulence. *J. Fluid Mech.*, **536**, 219–251, https://doi.org/10.1017/S0022112005004568.

Devenish, B., and Coauthors, 2012: Droplet growth in warm turbulent clouds. *Quart. J. Roy. Meteor. Soc.*, **138**, 1401–1429, https://doi.org/10.1002/qj.1897.

Duncan, K., B. Mehlig, S. Östlund, and M. Wilkinson, 2005: Clustering by mixing flows. *Phys. Rev. Lett.*, **95**, 240602, https://doi.org/10.1103/physrevlett.95.240602.

Earth Observing Laboratory, 2005: NSF/NCAR GV HIAPER aircraft. UCAR/NCAR, https://doi.org/10.5065/D6DR2SJP.

Frankel, A., G. Iaccarino, and A. Mani, 2017: Optical depth in particle-laden turbulent flows. *J. Quant. Spectrosc. Radiat. Transfer*, **201**, 10–16, https://doi.org/10.1016/j.jqsrt.2017.06.029.

Fugal, J., and R. Shaw, 2009: Cloud particle size distributions measured with an airborne digital in-line holographic instrument. *Atmos. Meas. Tech.*, **2**, 259–271, https://doi.org/10.5194/amt-2-259-2009.

Glienke, S., A. Kostinski, J. Fugal, R. A. Shaw, S. Borrmann, and J. Stith, 2017: Cloud droplets to drizzle: Contribution of transition drops to microphysical and optical properties of marine stratocumulus clouds. *Geophys. Res. Lett.*, **44**, 8002–8010, https://doi.org/10.1002/2017GL074430.

Gustavsson, K., S. Vajedi, and B. Mehlig, 2014: Clustering of particles falling in a turbulent flow. *Phys. Rev. Lett.*, **112**, 214501, https://doi.org/10.1103/physrevlett.112.214501.

Holtzer, G. L., and L. R. Collins, 2002: Relationship between the intrinsic radial distribution function for an isotropic field of particles and lower-dimensional measurements. *J. Fluid Mech.*, **459**, 93–102, https://doi.org/10.1017/S0022112002008169.

Ireland, P. J., A. D. Bragg, and L. R. Collins, 2016: The effect of Reynolds number on inertial particle dynamics in isotropic turbulence. Part 2. Simulations with gravitational effects. *J. Fluid Mech.*, **796**, 659–711, https://doi.org/10.1017/jfm.2016.227.

Jameson, A., and A. Kostinski, 2000: The effect of stochastic cloud structure on the icing process. *J. Atmos. Sci.*, **57**, 2883–2891, https://doi.org/10.1175/1520-0469(2000)057<2883:TEOSCS>2.0.CO;2.

Kendall, M., and A. Stuart, 1979: *The Advanced Theory of Statistics*. Vol. 2. Macmillan, 723 pp.

Kolmogorov, A., 1933: Sulla determinazione empirica di una legge di distribuzione. *G. Ist. Ital. Attuari*, **4**, 83–91.

Kostinski, A. B., 2001: On the extinction of radiation by a homogeneous but spatially correlated random medium. *J. Opt. Soc. Amer.*, **18A**, 1929–1933, https://doi.org/10.1364/JOSAA.18.001929.

——, and A. Jameson, 2000: On the spatial distribution of cloud particles. *J. Atmos. Sci.*, **57**, 901–915, https://doi.org/10.1175/1520-0469(2000)057<0901:OTSDOC>2.0.CO;2.

——, and R. A. Shaw, 2001: Scale-dependent droplet clustering in turbulent clouds. *J. Fluid Mech.*, **434**, 389–398, https://doi.org/10.1017/S0022112001004001.

Larsen, M. L., 2012: Scale localization of cloud particle clustering statistics. *J. Atmos. Sci.*, **69**, 3277–3289, https://doi.org/10.1175/JAS-D-12-02.1.

——, and A. S. Clark, 2014: On the link between particle size and deviations from the Beer–Lambert–Bouguer law for direct transmission. *J. Quant. Spectrosc. Radiat. Transfer*, **133**, 646–651, https://doi.org/10.1016/j.jqsrt.2013.10.001.

——, C. A. Briner, and P. Boehner, 2014: On the recovery of 3D spatial statistics of particles from 1D measurements: Implications for airborne instruments. *J. Atmos. Oceanic Technol.*, **31**, 2078–2087, https://doi.org/10.1175/JTECH-D-14-00004.1.

——, R. A. Shaw, A. B. Kostinski, and S. Glienke, 2018: Fine-scale droplet clustering in atmospheric clouds: 3D radial distribution function from airborne digital holography. *Phys. Rev. Lett.*, **121**, 204501, https://doi.org/10.1103/physrevlett.121.204501.

Lehmann, K., H. Siebert, M. Wendisch, and R. A. Shaw, 2007: Evidence for inertial droplet clustering in weakly turbulent clouds. *Tellus*, **59B**, 57–65, https://doi.org/10.1111/j.1600-0889.2006.00229.x.

Marshak, A., Y. Knyazikhin, M. Larsen, and W. J. Wiscombe, 2005: Small-scale drop size variability: Empirical models for drop-size-dependent clustering in clouds. *J. Atmos. Sci.*, **62**, 551–558, https://doi.org/10.1175/JAS-3371.1.

Matsuda, K., R. Onishi, R. Kurose, and S. Komori, 2012: Turbulence effect on cloud radiation. *Phys. Rev. Lett.*, **108**, 224502, https://doi.org/10.1103/physrevlett.108.224502.

——, ——, M. Hirahara, R. Kurose, K. Takahashi, and S. Komori, 2014: Influence of microscale turbulent droplet clustering on radar cloud observations. *J. Atmos. Sci.*, **71**, 3569–3582, https://doi.org/10.1175/JAS-D-13-0368.1.

Pinsky, M., and A. P. Khain, 2001: Fine structure of cloud droplet concentration as seen from the fast-FSSP measurements. Part I: Method of analysis and preliminary results. *J. Appl. Meteor.*, **40**, 1515–1537, https://doi.org/10.1175/1520-0450(2001)040<1515:FSOCDC>2.0.CO;2.

——, and ——, 2003: Fine structure of cloud droplet concentration as seen from the fast-FSSP measurements. Part II: Results of in situ observations. *J. Appl. Meteor.*, **42**, 65–73, https://doi.org/10.1175/1520-0450(2003)042<0065:FSOCDC>2.0.CO;2.

Pruppacher, H., and J. Klett, 2010: *Microphysics of Clouds and Precipitation*. 2nd ed. Springer, 954 pp.

Reade, W., and L. Collins, 2000: Effect of preferential concentration on turbulent collision rates. *Phys. Fluids*, **12**, 2530–2540, https://doi.org/10.1063/1.1288515.

Salazar, J., J. D. Jong, L. Cao, C. Woodward, H. Meng, and L. Collins, 2008: Experimental and numerical investigation of inertial particle clustering in isotropic turbulence. *J. Fluid Mech.*, **600**, 245–256, https://doi.org/10.1017/S0022112008000372.

Saw, E.-W., R. Shaw, S. Ayyalasomayajula, P. Chuang, and A. Gylfason, 2008: Inertial particle clustering of particles in high-Reynolds-number turbulence. *Phys. Rev. Lett.*, **100**, 214501, https://doi.org/10.1103/physrevlett.100.214501.

——, J. Salazar, L. Collins, and R. Shaw, 2012a: Spatial clustering of polydisperse inertial particles in turbulence: I. Comparing simulation with theory. *New J. Phys.*, **14**, 105030, https://doi.org/10.1088/1367-2630/14/10/105030.

——, R. Shaw, J. Salazar, and L. Collins, 2012b: Spatial clustering of polydisperse inertial particles in turbulence: II. Comparing simulation with experiment. *New J. Phys.*, **14**, 105031, https://doi.org/10.1088/1367-2630/14/10/105031.

Schmidt, L., I. Fouxon, and M. Holzner, 2017: Inertial particles distribute in turbulence as Poissonian points with random intensity inducing clustering and supervoiding. *Phys. Rev. Fluids*, **2**, 074302, https://doi.org/10.1103/physrevfluids.2.074302.

Scott, W., 1967: Poisson statistics in distribution of coalescing droplets. *J. Atmos. Sci.*, **24**, 221–225, https://doi.org/10.1175/1520-0469(1967)024<0221:PSIDOC>2.0.CO;2.

Shaw, R., A. Kostinski, and M. Larsen, 2002: Towards quantifying droplet clustering in clouds. *Quart. J. Roy. Meteor. Soc.*, **128**, 1043–1057, https://doi.org/10.1256/003590002320373193.

Siebert, H., S. Gerashchenko, A. Gylfason, K. Lehmann, L. Collins, R. Shaw, and Z. Warhaft, 2010: Towards understanding the role of turbulence on droplets in clouds: In situ and laboratory measurements. *Atmos. Res.*, **97**, 426–437, https://doi.org/10.1016/j.atmosres.2010.05.007.

——, R. Shaw, J. Ditas, T. Schmeissner, S. Malinowski, E. Bodenschatz, and H. Xu, 2015: High-resolution measurement of cloud microphysics and turbulence at a mountaintop station. *Atmos. Meas. Tech.*, **8**, 3219–3228, https://doi.org/10.5194/amt-8-3219-2015.

Skellam, J., 1946: The frequency distribution of the difference between two Poisson variates belonging to different populations. *J. Roy. Stat. Soc.*, **109A**, 296, https://doi.org/10.2307/2981372.

Spuler, S. M., and J. P. Fugal, 2011: Design of an in-line, digital holographic imaging system for airborne measurement of clouds. *Appl. Opt.*, **50**, 1405–1412, https://doi.org/10.1364/AO.50.001405.

Srivastava, R., 1989: Growth of cloud drops by condensation: A criticism of currently accepted theory and a new approach. *J. Atmos. Sci.*, **46**, 869–887, https://doi.org/10.1175/1520-0469(1989)046<0869:GOCDBC>2.0.CO;2.

Sundaram, S., and L. Collins, 1997: Collision statistics in an isotropic particle-laden turbulent suspension. Part 1. Direct numerical simulations. *J. Fluid Mech.*, **335**, 75–109, https://doi.org/10.1017/S0022112096004454.

Uhlig, E.-M., S. Borrmann, and R. Jaenicke, 1998: Holographic in-situ measurements of the spatial droplet distribution in stratiform clouds. *Tellus*, **50B**, 377–387, https://doi.org/10.3402/tellusb.v50i4.16210.